Available online at www.sciencedirect.com

SciVerse ScienceDirect

Acta Materialia 61 (2013) 1284–1293

Acta MATERIALIA

www.elsevier.com/locate/actamat

Mechanical and magnetocaloric properties of Gd-based amorphous microwires fabricated by melt-extraction

F.X. Qin [a,*], N.S. Bingham [b], H. Wang [c], H.X. Peng [a], J.F. Sun [c], V. Franco [d], S.C. Yu [e], H. Srikanth [b], M.H. Phan [b,*]

[a] *Advanced Composite Center for Innovation and Science, Department of Aerospace Engineering, University of Bristol, University Walk, Bristol BS8 1TR, UK*
[b] *Department of Physics, University of South Florida, Tampa, FL 33620, USA*
[c] *School of Materials Science and Engineering, Harbin Institute of Technology, Harbin 150001, China*
[d] *Dpto. Fısica de la Materia Condensada, ICMSE-CSIC, Universidad de Sevilla, PO Box 1065, 41080 Sevilla, Spain*
[e] *Department of Physics, Chungbuk National University, Cheongju 361-763, South Korea*

Received 29 July 2012; received in revised form 6 November 2012; accepted 6 November 2012
Available online 4 December 2012

Abstract

We report a systematic study of a new class of melt-extracted $Gd_{53}Al_{24}Co_{20}Zr_3$ amorphous microwires in terms of fabrication, structural characterization and evaluation of mechanical and magnetic properties. The tensile properties of the wires are characterized by a precision video gauge method and analyzed using the Weibull and lognormal methods. The three-parameter Weibull model and lognormal model based on the median rank value show consistent results and prove to be superior to the two-parameter Weibull model for the studied microwire with a smaller variation. The statistical mean tensile strength and fracture strain are calculated to be ~1200 MPa and ~2.0%, respectively, which are comparable with those of other metallic glasses. Remarkably, the microwires exhibit a large and reversible magnetocaloric effect (MCE), with the isothermal magnetic entropy change ($-\Delta S_m$) and refrigerant capacity (RC) reaching the large values of 5.32 J kg^{-1} K^{-1} and 467 J kg^{-1} for a field change of 3 T. Albeit with a low Curie temperature, these values are superior to those reported for pure Gd and other Gd-based bulk or ribbon-shaped glasses. The mean field model-based and Langevin function analyses reveal that the second-order magnetic transition behavior of the studied wire originates from the local anisotropy associated with the fine size of the wire and derogation and fluctuation of the exchange integral. These results demonstrate the adaptability and overall excellence of the newly developed Gd-based microwires, making them multifunctional elements for MCE-based cooling applications, especially for liquid nitrogen liquefaction.

Keywords: Melt-extraction; Amorphous microwires; Magnetocaloric effect

1. Introduction

Modern society relies very much on effective refrigeration. The currently prevailing technique, including vapor compression refrigerators, cannot meet the standard of high efficiency and, worse still, can jeopardize human life with the usage of dangerous gases, such as chlorofluorocarbons and hydro-chlorofluorocarbons [1–4]. Therefore, it is necessary to develop alternative techniques to circumvent these issues. Magnetic refrigeration based on the magnetocaloric effect (MCE), among others, emerges as one of the most promising techniques in view of its high efficiency (~50% higher than a gas compression-based cooling technique), compact structure, cost-effectiveness and environmental friendliness [5–8]. By definition, MCE refers to a reversible change in temperature of a magnetic material in response to an adiabatic application (magnetization)

---

* Corresponding authors. Tel.: +44 (0) 117 331 5765 (F.X. Qin).
E-mail addresses: faxiang.qin@gmail.com (F.X. Qin), phanm@usf.edu (M.H. Phan).

1359-6454/$36.00 © 2012 Acta Materialia Inc. Published by Elsevier Ltd. All rights reserved.
http://dx.doi.org/10.1016/j.actamat.2012.11.006

or removal of external magnetic field (demagnetization), and can therefore be characterized by the adiabatic thermal change (ΔT_{ad}) or the isothermal magnetic entropy change (ΔS_{m}). From the cooling application standpoint, however, the refrigerant capacity (RC) is a more important figure of merit in evaluating the cooling efficiency of magnetocaloric (MC) materials. RC, which is often calculated as a numerical integration of $-\Delta S_{\mathrm{m}}(T)$ from the cold and hot end temperatures at half maximum of the $-\Delta S_{\mathrm{m}}(T)$ peak [2]. Therefore, it measures not only the cooling power of a magnetocaloric material but also the thermodynamic efficiency of the material [9]. In order to obtain large RC, the material needs both a large ΔS_{m} and a transition that spans a broad temperature interval. This is also a basic requirement to realize active magnetic refrigeration (AMR) [10]. Most efforts have been devoted to exploring first-order magnetic transition (FOMT) materials, such as $Gd_5(Ge_{1-x}Si_x)_4$ $(0.3 \leq x \leq 0.5)$ [11,12], $Gd_5Si_2Ge_{1.9}Fe_{0.1}$ [4], $MnFeP_{0.45}As_{0.55}$ [13], $MnAs_xSb_{1-x}$ [14], and $La(Fe,Si)_{13}$ [15] due to the very large ΔS_{m}. However, FOMTs occur over a narrow temperature interval and are often accompanied with considerable thermal and field hysteresis, which are undesirable for AMR [16]. In contrast to FOMT materials, second-order magnetic transition (SOMT) materials, albeit presenting a smaller ΔS_{m}, work over a broader temperature interval and hence can possess a larger RC in favor of Ericsson circulation [17] and negligible hysteresis losses [18]. It is therefore challenging to achieve both large ΔS_{m} (or ΔT_{ad}) and large RC in a single material. A plausible solution for this could be exploring MCE in composite materials [19–22] that exhibit multiple SOMT temperatures and significantly enlarge RC by transforming the caret-like or ”λ”-shaped MCE profiles of single phase to table-like characteristics. Alternatively, one can design a regenerator bed containing different MC materials, constituting a graded cooling system [5]. In the latter case, the fine size of the MC materials applied is crucial as (i) it is in favor of high cooling efficiency with respect to size of the whole regenerator and (ii) it provides an additional freedom to control the amount and distribution of the MC materials in the regenerator bed, thus optimizing the cooling performance of the device.

In another perspective, metallic glasses have been extensively studied due to their exceptional overall performance in MCE resulting from the following advantages [23,24]: high electrical resistivity (small eddy current loss), high corrosion resistance, broadening of magnetic phase transition (absence of long-range order), excellent tunability of MCE and Curie temperature T_c by alloying, low hysteresis loss (good soft ferromagnetic properties) and good mechanical properties. The most studied metallic glasses are heavy rare-earth based, including Gd, Tb, Dy, Ho and Er, in that they have large magnetic moment ($Ng\mu_B\sqrt{J(J+1)}$) and total angular momentum quantum number (J), which determine the change in magnetic entropy according to [25]:

$$-\Delta S_m = \frac{Ng^2\mu_B^2 J(J+1)H^2}{3k_B(T-T_c)^2} \tag{1}$$

where N is the number of magnetic atoms per unit volume, g is the Landé factor, μ_B is the Bohr magneton (BM), and k_B is the Boltzmann constant. Among existing materials, gadolinium (Gd) shows an outstanding MCE performance near room temperature, which is often set as a baseline to evaluate newfound magnetocaloric materials [26]. However, pure Gd is rather expensive, so alloying it with other elements seems to be a unique way to find itself a niche in competitive refrigeration markets. Literature abounds on the MCE evaluation of amorphous materials in bulk and ribbon forms [27–35]. However, only a few works have reported on the MCE in amorphous wires [36]. Most recently, a numerical study performed by Vuarnoz et al. [10] revealed that an AMR system consisting of stacks of Gd wires, arranged parallel to the direction of heat transfer, show a good cooling performance. However, the large diameter of these wires limits the heat exchange surface area. While the authors suggested that the diameter of the wires should not be made thinner than 2.5 mm as the geometrical restriction of the wire would result in its poor mechanical properties, their calculation reveals an important consequence that the wires are a better option than particles of the same diameter with an increase of 30% in packing factor, twice larger pressure drop and higher coefficient of performance to implement in a magnetic bed of an AMR system. An inspiring conclusion was made that the AMR containing the stack of wires tends to increase the temperature span between its ends, which is of practical importance for realizing a higher cooling load with a higher efficiency.

In this context, capitalizing on recent progress in melt-extracted microwires [37–39], we have fabricated a new class of Gd-based microwires and systematically characterized their structural, mechanical and magnetocaloric properties. The results obtained cast great promises on the application of these micro-sized wires and the multiphase materials based on them for AMR applications.

2. Experimental

Amorphous wires of a nominal composition $Gd_{53}Al_{24}Co_{20}Zr_3$ were fabricated using a home-built melt-extraction facility as schematically shown in Fig. 1a. The composition is chosen as its bulk glass shows excellent MCE properties [31]. The detailed fabrication process is briefed here as follows. The ingot with a diameter of 8 mm was prepared from raw materials Gd (99.9%), Al (99.99%), Co (99.99%) and Zr (99.9%) crystals in argon atmosphere by arc melting. The melt extraction process was performed using a copper wheel with diameter of 160 mm and 60° knife edge, with a linear velocity of the wheel rim fixed at 30 m min^{-1} and a feed rate of the molten material of 90 μm s^{-1}. The appearance of obtained wire bundles is

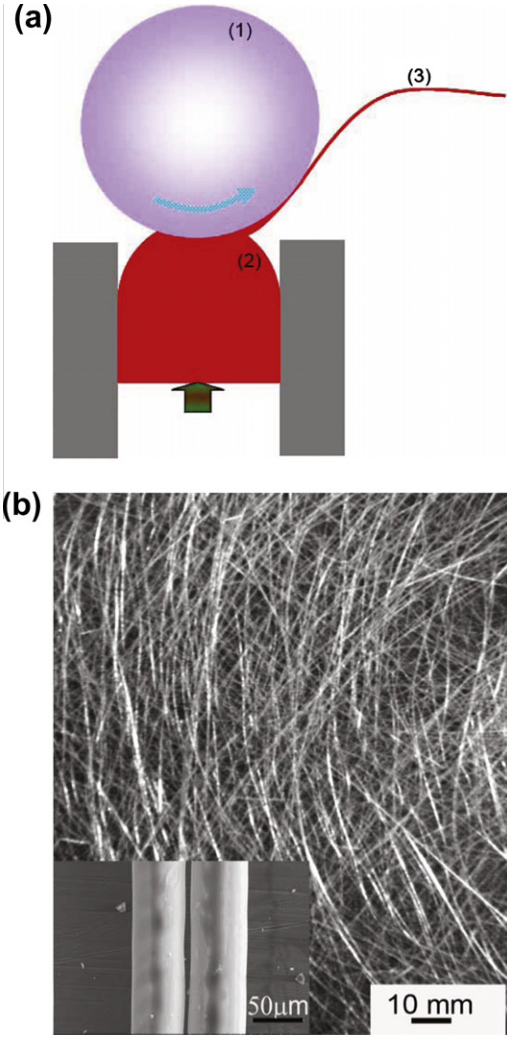

Fig. 1. (a) Schematic of a melt-extraction setup, where (1) indicates the spinning wheel, (2) is the melt puddle and (3) represents the extracted amorphous wires. (b) Optical graph of the fabricated wire bundles and the inset shows a side-view SEM image of the wires.

shown in Fig. 1b. The morphology of wires was observed by a field emission scanning electron microscope (SEM S-4700) at 15 kV. Thermal analysis was carried out in a Perkin–Elmer differential scanning calorimeter (DSC) at a heating rate of 20 K min^{-1}. The amorphous nature of wires was further confirmed by the X-ray diffraction (XRD) characterization: the diffractogram was obtained by a PANalytical's Empyrean with Cu Ka radiation; the image of diffraction patterns was taken by an Xcalibur-2 diffractometer from Oxford Diffraction with a Sapphire-2 CCD detector. The tensile properties of microwires were tested by an Instron tensile tester (Instron 3343) with a load cell of 10 N; the strain was measured by a video gauge. The magnetic measurements were performed using a commercial Physical Property Measurement System from Quantum Design in the temperature range of 2–350 K for applied fields up to 7 T.

3. Results and discussion

3.1. Structural characterization

The XRD profile and DSC trace obtained from the as-extracted $Gd_{53}Al_{24}Co_{20}Zr_3$ wires are shown in Fig. 2. A typical broad halo pattern without visible crystalline peaks is observed at ~33°, together with the ring-shaped diffraction patterns as shown in the inset of Fig. 2, indicating that a fully amorphous state is formed. Using the XRD data, one can calculate the radial distribution function (RDF) using the following formula [40]:

$$RDF(r) = 4\pi r^2\rho(r) = 4\pi r^2\rho_a + \frac{2r}{\pi}\int_0^\infty s[I(s)-1]\sin srds \qquad (2)$$

where r denotes the real time position of any atoms, $\rho(r)$ denotes the density of atoms at a distance of r from the origin. ρ_a denotes the average the density of atoms. $|s| = 4\pi\sin(\theta)/\lambda$ with θ representing half the diffraction angle and the X-ray wavelength $\lambda = 1.54$ Å. The coordination number of the outmost shell can then be numerically integrated from the first peak (not shown here): $Z = 11$, which is pretty close to the typical value of 12 for metallic glasses [41]. This critical parameter permits one to calculate the exchange integral through the $M(T)$ measurement, which will be discussed later. The amorphous nature of the wire is further confirmed from its DSC trace. As shown in the left inset of Fig. 2, the DSC trace exhibits a visible endothermic reaction due to the glass transition followed by two obvious crystallization (exothermic) peaks. The crystallization time and average rate are estimated to be ~480 s and 3.96×10^{-3} s^{-1}, which are typical for metallic glasses [42]. As indicated by the arrows, the glass transition

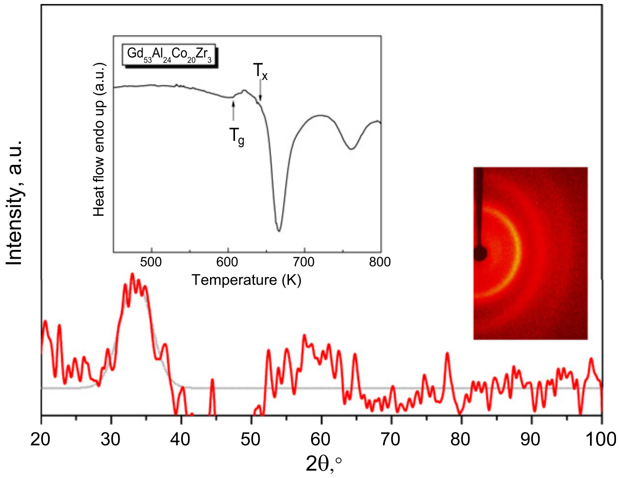

Fig. 2. XRD patterns of the wires with the diffraction patterns shown in the right inset and the left inset shows the DSC trace of the wire with the glass transition temperature T_g and crystallization onset temperature T_x indicated by the up and down arrows, respectively.

temperature T_g and crystallization onset temperature T_x are 606 K and 642 K ($\Delta T_x = T_x - T_g = 36$ K), respectively. It should be noted that the DSC curve of the present microwire is similar to that reported for its bulk counterpart [28], suggesting that the wire format does not alter much the glass forming ability (GFA) of the material. However, as compared to $Gd_{60}Al_{10+x}Co_{30-x}$ ($x = 0, 5, 10, 15$), which shows much a much larger ΔT_x (40–52 K), the addition of Zr does not enhance the GFA as what happened to FeNbAlBZr [43]. This can be understood from the three empirical rules proposed by Inoue [44], i.e., (1) multicomponent, (2) significant atomic size mismatches and (3) negative heats of mixing. The atomic radii of Gd, Al, Co and Zr are 0.178, 0.143, 0.125 and 0.16 nm. Al benefits the GFA with a medium atomic size which enables itself to insert into the inter-atomic spaces between Gd and Co. Likewise, the diameter of Zr is also between that of Gd and Co. In comparison with Al, Zr is much closer to that of Gd in diameter; it therefore makes no further contribution as Al does to diminish the overall diameter mismatch extent. As such, one would not expect a more reinforced backbone structure constituted by networking large and small atoms [45]. By contrast, the addition of elements of larger atomic radius, such as Zr to FeNbAlB or smaller radius such as Si to GdAlCo proves to be effective in improving the GFA. In addition, the enthalpy of mixing is $-38\ \mathrm{kJ\ mol^{-1}}$ for the Gd–Al pair, $-22\ \mathrm{kJ\ mol^{-1}}$ for the Gd–Co pair, $-19\ \mathrm{kJ\ mol^{-1}}$ for the Co–Al pair and $9\ \mathrm{kJ\ mol^{-1}}$ for the Gd–Zr pair. The addition of Zr clearly violates Inoue's rule. On the other hand, the addition of Zr by just 3 at.% will not severely degrade the GFA. The advantages of Zr addition lies in its improvement of the exchange integral, but the excessive addition of Zr (>8–10%) may decrease the T_c by occupying the Gd atom sites. Thus, leading to precipitation of new nanocrystalline phases [43,46], which is detrimental to both forming of amorphous structure and to the associated soft magnetic properties, which can greatly impact the MCE.

3.2. Mechanical properties

As Gd–Al forms strong bonding with relatively large mixing enthalpy, as mentioned above, this quaternary alloy is expected to have good mechanical properties. Previous studies have shown that the compressive fracture strength and Young's modulus are 1180–1380 MPa and 60–70 GPa for Gd–Al–Co bulk metallic glasses, respectively [47]. As the direct output from the tensile machine is unreliable, and the strain gauge cannot be applied to fibers of such fine size, a non-contact method has to be used. Using a video gauge that is able to capture precisely the displacement of targeted points in the sample, the real strain profiles can be accurately obtained. In comparison with other non-contact methods, such as interferometric strain displacement gauge, digital image correlation and differential digital image tracking [48–50], the video gauge method, which has a simplified configuration, is much more flexible.

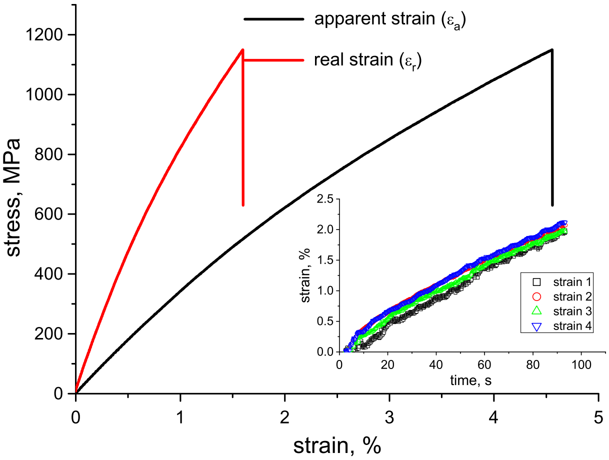

Fig. 3. Stress–strain curve of a specimen obtained from machine output (the case of apparent strain) and the video gauge (the case of real strain), respectively. The inset shows time dependence of four strain profiles recorded by the video gauge.

A detailed description of the facility and its reliabilities has been reported in previous studies [51,52]. Fig. 3 compares the results obtained from the apparent strain (output from the tensile tester) and real strain (from video gauge). The corrected (real) strain is only 35% of the apparent strain. We captured four points on the tested wires at an appreciable distance and four strain values were calculated from a built-in program. As shown in the inset in Fig. 3, the temporal response of strain shows an excellent consensus, demonstrating the reliability of the video gauge. We tested 19 specimens in total, prepared by fixing a wire of 10 mm gauge length in the middle of a frame made of cardboard. The short diameter, defined as the distance from free surface to droplet (as indicated by the arrow in the inset SEM image), averages 34.96 μm; its ratio to average long diameter (47.94 μm) is 0.713, which shows near semicircular geometry of the extracted sample. As pointed out by Inoue et al. [53], the geometry is determined by the processing parameters such as the wheel velocity and molten rising velocity; the roundness of the wires can therefore be improved by optimizing them. The average equivalent diameter (diameter of a circle with the same area as the cross-sectional area of the fiber) [54] is 41.25 (coefficient of variation: 9.1) μm and its distribution is shown in the inset of Fig. 4. Thus the tensile strength is calculated for each specimen. The stress data were statistically analyzed, as summarized in Table 1, and approached by the two-parameter Weibull method (TPWM), which is formulated as a two-parameter expression [55,56]:

$$P_f = 1 - e^{\left[-L\left(\frac{\sigma}{\sigma_0}\right)^m\right]} \tag{3}$$

where P_f is the Weibull cumulative distribution describing the probability of failure of a fiber of length L at a stress less than or equal to the stress σ, σ_0 is the characteristic stress (or Weibull scale parameter) and m is Weibull modulus (or shape parameter), which describes the variability

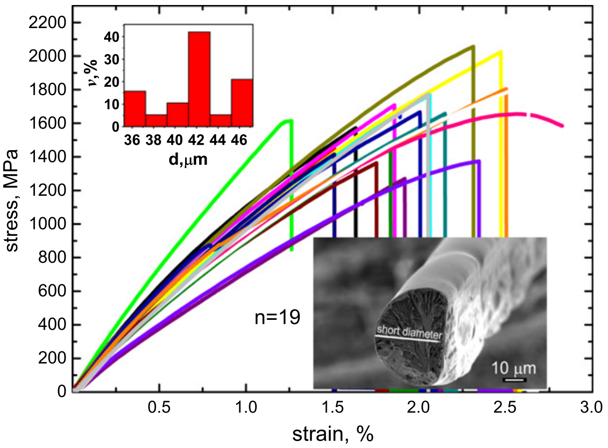

Fig. 4. Stress–strain curves of 19 specimens; the top inset is the distribution of equivalent diameter, v% is termed as the percentage of the samples in certain equivalent diameter of the wires (values of abscissa) out of the total number of tested samples; the bottom inset shows a cross-sectional view of the microwire with the short diameter indicated by the arrow from the free surface to the shaped flat surface in connection to the copper wheel.

of the failure strength. One can then extract these two parameters by plotting ln(ln(1/1 − P_f))) vs. ln(σ) as shown in Fig. 5a. Subsequently, one can compute the Weibull mean stress in the form of [57]:

$$\bar{\sigma} = \sigma_0 L^{-1/m} \Gamma\left(1 + \frac{1}{m}\right) \tag{4}$$

The parameters of the Weibull distribution were estimated through the linear regression method, using the following estimator (median rank value) [57]:

$$P_f = \frac{i - 0.3}{n + 0.4} \tag{5}$$

where i denote the rank of the ith data point and n is the number of data points.

For a more general case, one can apply the three-parameter Weibull model (TrPWM) by taking into account the failure threshold σ_{ft}, which is in the form of [58]

$$\ln\left[\ln\left(\frac{1}{1 - P_f}\right)\right] = m \ln(e^{\ln(\sigma)} - \sigma_{ft}) + \ln L - m \ln \sigma_0 \tag{6}$$

Like TPWM, TrPWM can also derive all parameters from the plot of ln(ln(1/(1-P_f))) vs. ln(σ). Note that when $\sigma_{ft} = 0$, Eq. (5) is reduced to TPWM form. Fig. 5a shows both fitting curves; the linear fit of TPWM is relatively poor with an R^2 of 0.83 and large Weibull modulus of 6.1. The mean strength calculates 1748 MPa, i.e., 7% deviation from the average stress value. These results demonstrate that the TPWM is somewhat indicative but not accurate By contrast, the TrPWM yields a good fit with an R^2 of 0.975 and small m of 1.22. The calculated failure threshold is 1219 MPa, which sets a reliably safe boundary of using the material, which is 75% of the average stress. Note that in some studies (e.g. Ref. [58]) p is defined as $p = (i - 0.5)/n$, which is not as accurate as the median rank value for the current case, which gave a rather poor fit (not shown here) with much larger m of 9.38 and considerably underestimating a mean stress of only 968 MPa.

Alternatively, the failure strengths of brittle materials are sometime described by a log-normal distribution, where the probability of failure is given by [59]:

$$P_{f,LN} = \frac{1}{2}\left[1 + erf\left(\frac{\ln(\sigma) - \kappa}{s\sqrt{2}}\right)\right] \tag{7}$$

where κ is the mean and s is the standard deviation of the natural log of the stress data. From the fitting curve (Fig. 5b), one can also calculate the average mean strength exp(7.122) = 1239 MPa, which is close to the value obtained by the TrPWM model, further confirming the validity of this stress value as an reliable evaluation parameter.

To put our discussion in context, we compare in Table 1 the tensile properties of the presently studied Gd-based

Table 1
Tensile properties of $Gd_{53}Al_{24}Co_{20}Zr_3$ microwire in comparison with other metallic glasses in microwires (m) and bulk format (b).

Microwire	Format	Tensile strength (MPa)	Young's modulus (GPa)	Fracture strain (%)	Failure threshold strength (MPa) lognormal strength	References
Gd-based	m	1622.74 ± 216.57	82.85 ± 15.42	2.01 ± 0.39	1219, 1239	Present work
Zr-based	m	1765	93.88	1.88		[60]
Pd-based	m	1306	67.67	1.93		[61]
Pd-based	m	1580	69.60	2.27		[61]
Ni-based	m	2300	100.00	2.3		[62]
Fe-based	m	3800	165.22	2.3		[63]
Co-based	m	3300	150.00	2.2		[64]
Go-based	m	3242	117.04	2.77		[64]
Go-based	m	3850	128.33	3		[64]
La-based	b	835.82	42.25	1.98		[47]
Mg-based	b	1149.25	60.92	1.89		[47]
Zr-based	b	1731.34	86.46	2.00		[47]
Pd-based	b	1656.72	86.46	1.92		[47]

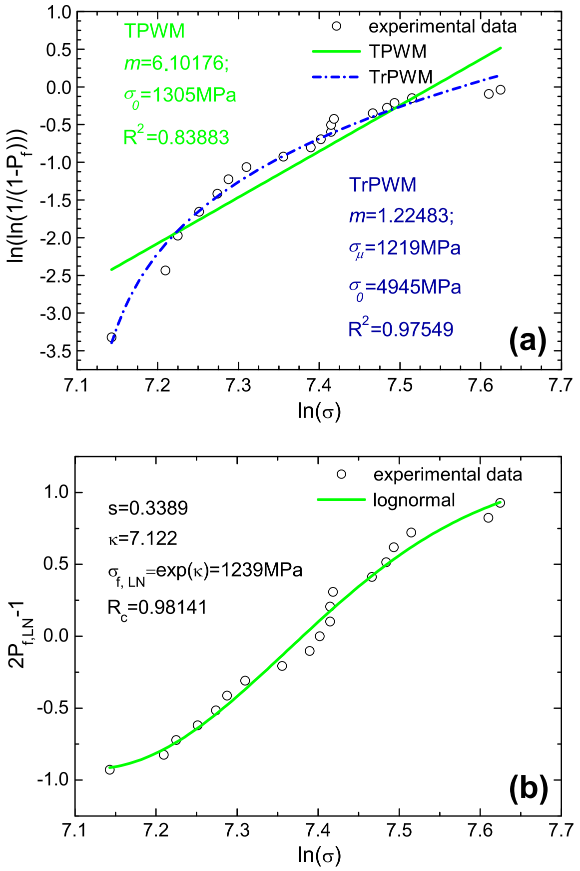

Fig. 5. (a) Weibull plots for tensile fracture strength of tested wires fitted by TPWM and TrPWM; (b) lognormal plots.

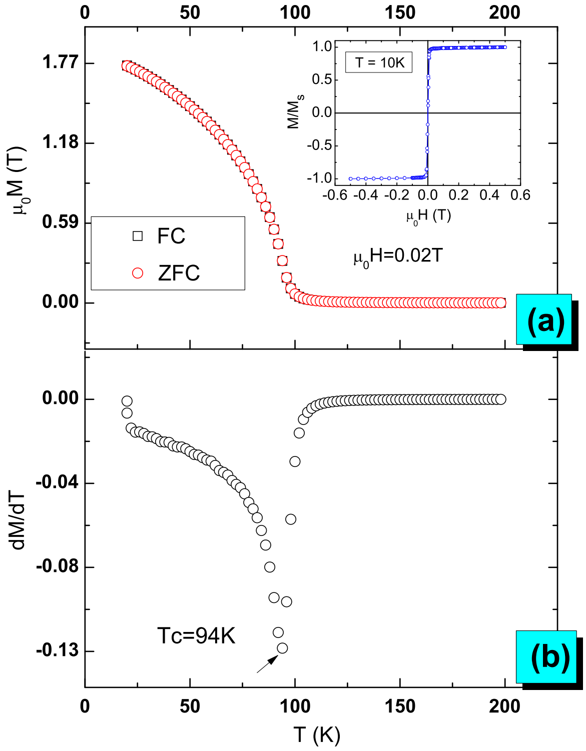

Fig. 6. (a) Temperature dependence of zero-field-cooled (ZFC) and field-cooled (FC) magnetization taken at a field of 0.02 T. The inset shows the M–H curve at $T = 10$ K. (b) Temperature dependence of the derivative of magnetization with respect to temperature (dM/dT).

wire with other metallic fibers. Overall, one can conclude from the testing results and statistical analyses thereof that the Gd-based wire has a reasonably good mechanical property: its tensile strength and Young's modulus are comparable to those of Zr-based and Pd-based alloys either in the microwire or bulk form, and higher than those of La-based and Mg-based bulk glasses, but much inferior to those of Fe- and Co-based microwires. The fracture stain is in the average level of all materials compared, which enables them to be geometrically adaptable to a diversity of cooling systems.

3.3. Magnetic and magnetocaloric properties

Zero-field-cooled and field-cooled measurements were carried out by cooling the specimen in zero magnetic field and a constant applied magnetic field, respectively, before the magnetization of the material is recorded on increasing temperature under the same applied magnetic field. It is expected that the zero field measurement is irreversible below the freezing temperature. The observation that the $M(T)$ is reversible in the whole measurement range of 10 to 200 K (Fig. 6a) indicates that there is no glass (cluster glass or spin glass) phase and that there is a single magnetic phase, i.e. ferromagnetic phase ($T < T_c$) for the studied microwire. This is different from the case of Mn-based bulk glasses, where Mn moments couple antiparallel to Gd moments, thus causing spin glasses [35]. The Curie temperature, determined from the inflection point of the $M(T)$ curve measured under 0.02 T is 94 K (Fig. 6b), which is much lower than that of the crystalline Gd (293 K). This can be attributed to the structural disordering and the addition of alloying elements, which impacts on the Ruderman–Kittel–Kasuya–Yosida (RKKY) magnetic interactions that govern the magnetic properties of RE-based intermetallics. For a Gd-based microwire, these interactions depend locally on two parameters, namely, Gd–Gd interatomic distances and the number of conduction electrons. As such, the composition and structure play a significant role in determining the magnetic behavior of the Gd-based wire.

To further understand the magnetic features of the studied wire, $M(H)$ data were fit by the Langevin function, as shown in Fig. 7. One can see a good fit to the experimental data at 95 K (close to T_c). The fit values of R^2 (0.999) close to unity suggest clearly that the studied magnetic behavior falls within the classical limit of a high magnetic moment. The fitting parameters confirm that Gd^{3+} clusters are formed with effective number of Bohr magnetons of $2.58\mu_B$/fu, which is much lower than that of the isolated Gd^{3+}($7\mu_B$/fu). This demonstrates that the paramagnetic (PM) phase has weak interactions of Gd^{3+}, which

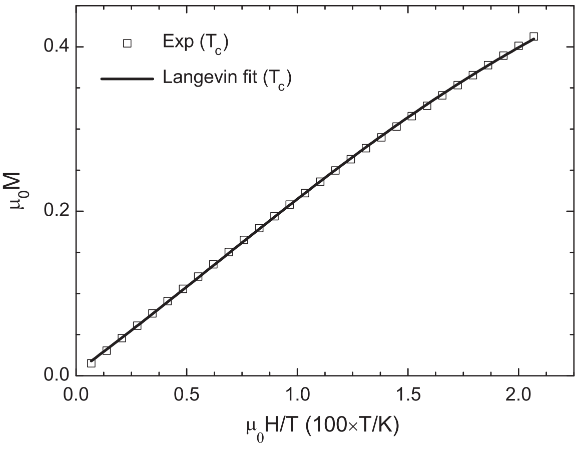

Fig. 7. Field to temperature ratio dependence of magnetization at 95 K that is close to the T_c; the experimental data are fitted by the Langevin functions with three parameters.

originates from the disordering effect, i.e., deterioration and fluctuation of the exchange integral [65]. One can then picture the evolution of magnetic features with temperature transition at each stage: At high temperature, the PM properties can be better described by Langevin function. Cooling below T_c makes the short-range exchange interactions dominate k_BT and the ordering clusters (group of spins) are formed (Fig. 7).

Isothermal field dependence of M was measured between 0 and 3 T, for various temperatures between 20 and 200 K. These $M(H)$ curves (Fig. 8a) allow calculating the isothermal magnetic entropy change by applying the thermodynamic Maxwell equation [25]:

$$\left(\frac{\delta S}{\delta H}\right)_T = -\left(\frac{\delta M}{\delta T}\right)_H \tag{8}$$

where S denotes the magnetic entropy. Following Eq. (8), the magnetic entropy change of the sample, ΔS_m, under demagnetization in isothermal process can be calculated by integrating over the magnetic field as follows [66]:

$$\Delta S_m = \int_0^H \left(\frac{\delta M(T,H)}{\delta T}\right)_H dH \tag{9}$$

The resulting ΔS_m vs. T plots under different magnetic field variations are displayed in Fig. 8c. As expected, with increasing magnetic field, $-\Delta S_m$ increases significantly along with a slight increase of T_p (equal to T_c in the present case), where the peak of $-\Delta S_m$ occurs. The peak values of $-\Delta S_m$ are 5.32 J kg^{-1} K^{-1} at 100 K for $H = 3$ T, which compares well with other MCE materials including Gd and GdSiGe series as summarized in Fig. 9. The most

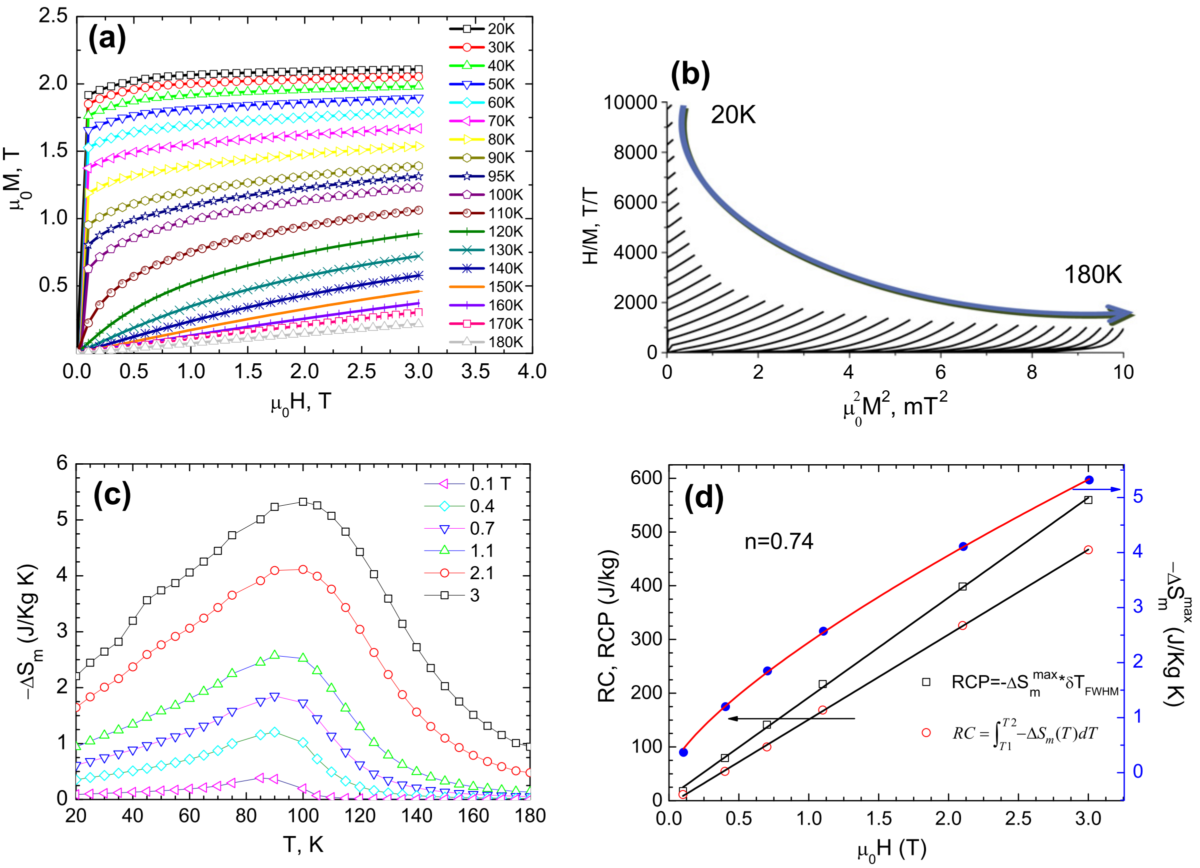

Fig. 8. (a) Isothermal magnetization as a function of magnetic field in a wide temperature range of 20–180 K. (b) Arrott plot for the studied wire from 20 to 180 K. (c) Magnetic entropy changes $-\Delta S_m$ under varying magnetic field variations. (d) H dependence of RC, RCP, and $-\Delta S_m^{max}$ for the studied wires.

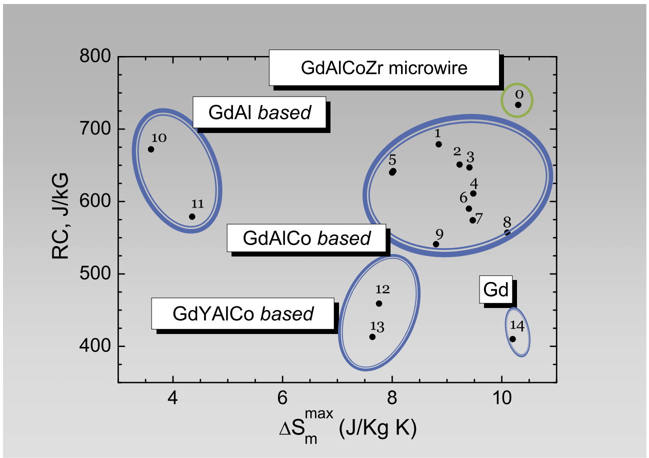

Fig. 9. RC w.r.t. $-\Delta S_m^{max}$ of a variety of bulk Gd-based metallic glasses in comparison with the studied $Gd_{53}Al_{24}Co_{20}Zr_3$ microwire.

remarkable feature is the broad peak of $-\Delta S_m$, indicating a desirable SOMT feature resulting from the disordered structure of the material, which is confirmed by the Arrott plot [67] exhibiting all positive slopes (a negative slope would indicate a FOMT) of H/M vs. M^2 (Fig. 8b). The broad peak feature can be further understood by computation of the heat capacity discontinuity at zero field (ΔC_m) at the Curie transition within the framework of the mean field theory. According to Liu et al. [68],

$$\Delta C_m \approx Nk_B \frac{5J(J+1)}{J^2+(J+1)^2} \tag{10}$$

By fitting the M–H data to Langevin function, $N = 1.15 \times 10^{23}$ mol^{-1}, $J = 3.5$ for Gd, giving $\Delta C_m = 3.514$ J mol^{-1} K^{-1}, which is large enough to induce an appreciable discontinuity of the second order phase transition. Note that although the J value for heavy rare earth elements is large enough to push the term of $J(J+1)/(J^2+(J+1)^2)$ to the maximum of 1/2, the weak interactions between Gd^{3+} depreciate the effective number of magnetic atoms from an ideal situation. This explains why ΔC_m fails to reach 14.1–14.4 J K^{-1} mol^{-1} as in Ref. [68], which considers the effective moment of Gd-based metallic glasses as $7\mu_B$.

Based on Fig. 8c, the field dependence of maximum entropy change ($-\Delta S_m^{max}$) is plotted to further understand the physics of the MCE response of the studied wire at transition temperature. As for SOMT materials, $-\Delta S_m^{max}$ (H) follows a scaling law, i.e. $-\Delta S_m^{max} \propto H^n$ [69]. As shown in Fig. 8d, the fitting of full circle points ($-\Delta S_m^{max}$) leads to that $n = 0.74$ for the studied Gd-based amorphous wire. As expected, it deviates from the value of 2/3 corresponding to mean field theory [70] due to the local inhomogeneities in the melt-extracted wire. The exponent value of 0.74 is close to 0.75, the typical value for Fe-based amorphous alloys [71–73]. We have demonstrated that the inhomogeneities could act as nucleation sites to induce the generation of nanocrystals and have a significant impact on the mechanical and magnetic properties of the wires [37]. The improvement of the homogeneity of the microwire via optimization of the fabrication process or post-processing can then improve the predictability of H dependence of MCE parameters.

The refrigerant capacity (RC) can be obtained by numerically integrating the area under the $\Delta S_m(T)$ curve using the temperatures at half maximum of the peak as the integration limits, i.e., $RC = \int_{T_1}^{T_2} -\Delta S_m(T)dT$. Note that researchers (e.g. Ref. [32]) also use the product of the peak entropy change and the full width at half maximum of the peak (strictly termed as relative cooling power (RCP)), i.e., $RCP = -\Delta S_m^{max}(T_2 - T_1)$ [6]; it is typically 4/3 of the RC as can be readily proved by approximating the area under the $-\Delta S_m(T)$ curve as a triangle. It is therefore important to make sure the RC is properly defined and unified to make a comparison meaningful. Fig. 8d shows an increase in both RCP and RC with increasing magnetic field. The RC value is also compared with other materials as shown in Fig. 9. Remarkably, it shows the superior MCE performance than its counterpart in bulk form. Intuitively, we understand that the magnetic properties of the microwires are expected to be different from those of their bulk counterpart. Based on the local anisotropy, the mobility of clusters in the microwires is size dependent, and a distribution of cluster sizes results in unique properties [23,74]. It is worth commenting that, although the studied Gd-wire exhibit both large RC and $-\Delta S_m$, its Curie temperature is much lower than pure Gd or many other metallic glasses [32], due to the twofold mechanisms: (i) the disorder effect significantly reduces the electron mean free path and in consequence decreases the RKKY coupling at a smaller length scale [75]; (ii) According to Weiss mean field theory, $T_c = 2ZA_{ex}J(J+1)/3k_B$ [41], a weak interaction between Gd, as the dominant magnetic elements, leads to the relatively low T_c of its alloy. But note that it does not necessarily mean the Gd-based metallic glass has low T_c, as the electronic configuration of the transition elements can significantly influence T_c. Specifically, assuming all elements are alloyed with a concentration over the critical value of being magnetic, if one exchanges Co for Mn or Fe (Cu or Ni, respectively), which the ion will have larger (smaller, resp.) number of Bohr magnetons, the T_c will be generally tuned higher (lower, resp.).

4. Conclusions

A thorough study of the structural, mechanical and magnetic properties of the melt-extracted $Gd_{53}Al_{24}Co_{20}Zr_3$ microwires has been performed. The microwire shows good glass forming ability and thermal stability. The competitive mechanical properties were presented based on a detailed statistical analysis on a number of specimens. The three-parameter Weibull model and Lognormal model fit well with the experimental data with a statistical strength of 1219 and 1239 MPa, respectively. The fracture stain of 2.1% obtained from a non-contact video gauge compares well with other metallic amorphous materials, which enable them to be geometrically adaptable to a diversity of cooling systems. The microwires exhibited an excellent MCE performance with the $-\Delta S_m^{\max}$ and RC values of 5.32 J kg^{-1} K^{-1} and 467 J kg^{-1} for a field change of 3 T, respectively, thus distinguishing them from other metallic glasses. The overall SOMT behavior originates from the formation of magnetic clusters due to the competition between the development of the short-range spatial magnetic ordering and the disordering effect of the random magnetic anisotropy. The disordering effect has been analysed by the mean field model-based and Langevin function methods. It appears that the local anisotropy associated with the fine size of the wire significantly improves the MCE. Therefore, tuning the strength of the random anisotropy, for example, through heat treatment or doping allows one to tailor the magnetic properties and MCE of amorphous alloys. An innovative application of the studied Gd-based microwires in AMR is promised by realizing the following two critical factors: (i) mechanically adaptable to various cooling systems and (ii) reduction of the wire diameter in favor of a large coefficient of performance. Thus a graded MCE composite material containing these microwires can be realized, and design and fabrication of which is under way.

Acknowledgements

FXQ is supported by the EPSRC institutional sponsorship. HW is grateful to the financial support from the short-term doctoral visiting scholar program of Harbin Institute of Technology. M.H.P. and H.S. acknowledge support from the Department of Army through Grant No. W911NF-08-1-0276 and the Florida Cluster for Advanced Smart Sensor Technologies (FCASST). VF acknowledges the support of the Spanish Ministry of Science and Innovation and EU FEDER (Project MAT2010-20537), the PAI of the Regional Government of Andalucía (Project P10-FQM-6462), and the United States Office of Naval Research (Project N00014-11-1-0311). SCY acknowledges support from the Converging Research Center Program funded by the Ministry of Education, Science and Technology (2012K001431). The authors would also like to thank Dr. François Michaud of Université de Bretagne Occidentale for the help with XRD characterization.

Compounds legend for Fig. 9

0. $Gd_{53}Al_{24}Co_{20}Zr_3$ microwire [current work]	1.$Gd_{51}Al_2Co_{20}Ce_5$ [76]	2. $Gd_{51}Al_{24}Co_{20}Zr_4Nb_1$ [77]
3. $Gd_{48}Al_{25}Co_{20}Zr_3Er_4$ [77]	4. $Gd_{51}Al_{24}Co_{20}Nb_1Cr_4$ [77]	5.$Gd_{37}Tb_{26}Co_{20}Al_{22}$ [33]
6. $Gd_{53}Al_{24}Co_{20}Zr_3$ [31]	7. $Gd_{33}Al_{25}Co_{20}Er_{22}$ [31]	8. $Gd_{60}Co_{26}Al_{14}$ [77]
9. $Gd_{55}Co_{20}Al_{25}$ [17]	10. $Gd_{60}Fe_{30}Al_{10}$ [78]	11. $Gd_{55}Fe_{20}Al_{25}$ [79]
12.$Gd_{36}Y_{20}Al_{24}Co_{20}$ [80]	13 $Gd_{30}Al_{25}Co_{20}Y_{20}Zr_5$ [76]	14 Gd [3]

References

[1] Ekkes BJ. Phys D Appl Phys 2005;38:R381.
[2] GschneidnerJr KA, Pecharsky VK, Tsokol AO. Rep Prog Phys 2005;68:1479.
[3] Phan M-H, Yu S-C. J Magn Magn Mater 2007;308:325.
[4] Provenzano V, Shapiro AJ, Shull RD. Nature 2004;429:853.
[5] Nielsen KK, Tusek J, Engelbrecht K, Schopfer S, Kitanovski A, Bahl CRH, et al. Int J Refrig 2011;34:603.
[6] Gschneidner KA, Pecharsky VK. Annu Rev Mater Sci 2000;30:387.
[7] Phan MH, Yu SC. Magnetoresistance, magnetoimpedance and magnetocaloric phenomena in ferromagnetic manganites. Handbook of ceramic materials research trends. Hauppauge, New York: Nova Science Publishers; 2007. p. 43.
[8] Franco V, Blázquez JS, Ingale B, Conde A. Ann Rev Mater Res 2012;42:305.
[9] Wood ME, Potter WH. Cryogenics 1985;25:667.
[10] Vuarnoz D, Kawanami T. Appl Therm Eng 2012;37:388.
[11] Pecharsky VK, Gschneidner JKA. Phys Rev Lett 1997;78:4494.
[12] Choe W, Pecharsky VK, Pecharsky AO, Gschneidner Jr KA, Young Jr VG, Miller GJ. Phys Rev Lett 2000;84:4617.
[13] Wada H, Tanabe Y. Appl Phys Lett 2001;79:3302.
[14] Tegus O, Bruck E, Buschow KHJ, de Boer FR. Nature 2002;415:150.
[15] Fujieda S, Fujita A, Fukamichi K. Appl Phys Lett 2002;81:1276.
[16] Hui X-D, Xu Z-Y, Wang E-R, Chen G-L, Lu Z-P. Chin Phys Lett 2010:27.
[17] Du J, Zheng Q, Li YB, Zhang Q, Li D, Zhang ZD. J Appl Phys 2008;103:023918.
[18] Tishin AM, Spichkin YI. The magnetocaloric effect and its applications. Bristol: Institute of Physics Publishing; 2003.
[19] Smaili A, Chahine R. J Appl Phys 1997;81:824.
[20] Chaturvedi A, Stefanoski S, Phan M-H, Nolas GS, Srikanth H. Appl Phys Lett 2011;99:162513.
[21] Caballero-Flores R, Franco V, Conde A, Knipling KE, Willard MA. Appl Phys Lett 2011;98:102505.
[22] Paticopoulos SC, Caballero-Flores R, Franco V, Blázquez JS, Conde A, Knipling KE, et al. Solid State Commun 2012;152:1590.
[23] Giguere A, Foldeaki M, Dunlap RA, Chahine R. Phys Rev B 1999;59:431.
[24] Franco V, Conde A. Scr Mater 2012;67:594.
[25] Hashimoto T, Numasawa T, Shino M, Okada T. Cryogenics 1981;21:647.
[26] Gschneidner KA, Pecharsky VK. Int J Refrig 2008;31:945.
[27] Li Q, Cai P, Shen B, Makino A, Inoue A. Journal of magnetics 2011;16:440.
[28] Zhang CL, Wang DH, Han ZD, Xuan HC. J Appl Phys 2012;105:013912.
[29] Dong QY, Shen BG, Chen J, Shen J. J Appl Phys 2009;105:053908.
[30] Du J, Zheng Q, Li YB, Zhang Q, Li D, Zhang ZD. J. Appl. Phys. 2008;103:023918.
[31] Luo Q, Zhao DQ, Pan MX, Wang WH. Appl Phys Lett 2006;89:081914.

[32] Fang YK, Chen HC, Hsieh CC, Chang HW, Zhao XG, Chang WC, et al. J Appl Phys 2011;109(07):A933.
[33] Liu Y, Zhang J, Wang Y, Zhu Y. Appl Phys Lett 2009;94:112507.
[34] Mayer C, Chevalier B, Gorsse S. J Alloys Compd 2010;507:370.
[35] Mayer C, Ballon G, Caballero-flores R. J Appl Phys 2011;110:053920.
[36] Ilyn MI, Zhukova V, Santos JD, Prida VM, Hernando B, Larin V, et al. Phys. Status Solidi A 2008;1381:1378.
[37] Wang H, Xing D, Peng H, Qin F, Cao F, Wang G, et al. Scripta Mater 2012;66:1041.
[38] Wang H, Xing D, Wang X, Sun J. Metall Mater Trans A 2010;42:1103.
[39] Wang H, Qin FX, Xing D, Cao F, Wang XD, Peng H, et al. Acta Mater 2012;60:5425.
[40] Qin L-C. In: Zhang XF, Zhang Z, editors. Progress in transmission electron microscopy concepts and techniques, vol. 38. New York: Springer-Verlag/TUP; 2001. p. 223.
[41] Patterson JD, Bailey BC. Solid-state physics: introduction to the theory. Berlin/Heidelberg: Springer; 2007.
[42] Koster U, Schunemarm U, Blank-Bewersdorff M. Mater Sci Eng A 1991;133:611.
[43] Bai Q, Xu H, Tan X-H, Meng T. Chin Phys Lett 2009;26:057503.
[44] Inoue A, Zhang T, Zhang W, Takeuchi A. Mater Trans JIM 1996;37:99.
[45] Poon SJ, Shiflet GJ, Guo FQ, Ponnambalam V. J Non-Cryst Solids 2003;317:1.
[46] Zhang SY, Xu H, Ni JS, Wang HL, Hou XL, Dong YD. Physica B 2007;393:153.
[47] Chen D, Takeuchi A, Inoue A. Mater Sci Eng A 2007;457:226.
[48] Gianola DS, Eberl C. JOM J Min Met Mater Soc 2009;61:24.
[49] Huang H, Spaepen F. Acta Mater 2000;48:3261.
[50] Gianola DS, Eberl C, Cheng XM, Hemker KJ. Adv Mater 2008;20:303.
[51] Towse A, Potter K, Wisnom MR, Adamsà RD. J Mater Sci 1998;33:4307.
[52] Daynes S, Potter K, Weaver P. Compos Sci Technol 2008;68:3431.
[53] Inoue A. Acta Mater 2000;48:279.
[54] Kostronov AG, Klimenko VN, Serov MM, Levitskii NI, Prishchepov SV, Borisov BV. Powder Metall 2008;47:384.
[55] Weibull W. Appl Mech 1951;18:293.
[56] Pickering KL, Murray TL. Science 1999;30:1017.
[57] Rosa IMD, Puglia D, Santulli C, Sarasini F. J Reinf Plast Compos 2010;29:3450.
[58] Gao H-l, Shen Y, Xu J. Introduction I 2011:2087.
[59] Pulskamp J, Gianola DS, Eberl C, Polcawich RG, Thompson RJ. Exp Mech 2007:649.
[60] Yi J, Xia XX, Zhao DQ, Pan MX, Bai HY, Wang WH. Adv Eng Mater 2010;12:1117.
[61] Inoue A, Masumoto Y, Yano N, Kawashima A, Hashimoto KTM. J Mater Sci 1985;20:97.
[62] Nagase T, Ueda M, Umakoshi Y. J Alloy Compd 2009;485:304.
[63] Waseda Y, Ueno S, Hagiwara M, Aust K. Prog Mater Sci 1990;34:149.
[64] Wu Y, Li HX, Chen GL, Hui XD, Wang BY, Lu ZP. Scr Mater 2009;61:564.
[65] Xu ZY, Hui X, Wang ER, Chang J, Chen GL. J Alloys Compd 2010;504S:S146.
[66] Morrish AH. The physical principles of magnetism. New York: Wiley; 1965.
[67] Banerjee SK. Phys Lett 1964;12:16.
[68] Liu XY, Barclay JA, Gopal RB, Fodeaki M, Chahine R, Bose TK, et al. J Appl Phys 1996;79:1630.
[69] Franco V, Conde A. Int J Refrig 2010;33:465.
[70] Oesterreicher H, Parker FT. J Appl Phys 1984;55:4334.
[71] Franco V, Borrego JM, Conde CF, Conde A. J Appl Phys 2006;100:083903.
[72] Franco V, Borrego JM. J Appl Phys 2007;101(09):C503.
[73] Franco V, Conde A. Appl Phys Lett 2006;89:222512.
[74] Marchand A, Devaux X, Barbara B, Mollard P, Brieu M, Rousset A. J Mater Sci 1993;28:2217.
[75] Gorsse S, Orveillon G, Chevalier B. J Appl Phys 2008;103:044902.
[76] Luo Q, Wang WH. J Alloys Compd 2010;495:209.
[77] Wang W. Adv Mater 2009;21:4524.
[78] Schwarz B, Podmilsak B, Mattern N, Eckert J. J Magn Magn Mater 2010;322:2298.
[79] Yuan F, Li Q, Shen B. J Appl Phys 2012;111(07):A937.
[80] Liang L, Hui X, Wu Y, Chen GL. J Alloys Compd 2008;457:541.